International Journal of Mass Spectrometry 495 (2024) 117165

Contents lists available at ScienceDirect

International Journal of Mass Spectrometry

journal homepage: www.elsevier.com/locate/ijms

IR spectroscopic characterization of products of methane and cyclopropane activation by Ru cations☆

Frank J. Wensink [a], Deepak Pradeep [a], P.B. Armentrout [b], Joost M. Bakker [a,*]

[a] Radboud University, Institute for Molecules and Materials, FELIX Laboratory, Toernooiveld 7, 6525ED, Nijmegen, the Netherlands
[b] University of Utah, Department of Chemistry, 315 South 1400 East, Room 2020, Salt Lake City, UT, 84112, United States

A B S T R A C T

Methane and cyclopropane (c-C_3H_6) were reacted with Ru^+ ions in a room temperature ion trap and the resulting products were identified using a combination of mass spectrometry, IR action spectroscopy, and density functional theory calculations. In the reaction with methane, no products with odd numbers of carbon atoms were located, whereas significant amounts of products with even numbers of carbon atoms were observed. We identified $[Ru,2C,4H]^+$ as the Ru^+ ion with an ethene ligand attached, and $[Ru,4C,6H]^+$ as a $Ru(\eta^4$-*cis*-1,3-butadiene$)^+$ complex. The barrier toward formation of $Ru(C_2H_4)^+ + 2H_2$ was calculated at the B3LYP/def2-TZVPPD level to be 0.80 eV above the energy of the ground state Ru^+ (^4F) + 2 CH_4 reactants. In the reaction of c-C_3H_6 with Ru^+, we identified the dehydrogenation product $[Ru,3C,4H]^+$ as $Ru(\eta^2$-propyne$)^+$, $[Ru,2C,2H]^+$ as Ru^+ with an ethyne ligand, and $[Ru,5C,5H]^+$ as $Ru(\eta^5$-c-$C_5H_5)^+$ having a cyclopentadienyl ligand.

1. Introduction

Methane is the primary component of natural gas, which is present abundantly on earth. Currently, the first step in natural gas conversion to value added products is the production of synthesis gas [1]. Syngas in turn can be converted into liquid hydrocarbons over an iron or cobalt based catalyst via Fischer–Tropsch synthesis (FTS) [2]. In both steps, large amounts of energy are used, making it desirable to explore ways of direct, more efficient methane utilization. Unfortunately, this is cumbersome because of the high stability of methane and the long-standing challenge to selectively activate sp^3 hybridized C–H bonds [3,4].

To better understand the activation chemistry of methane, its interaction with isolated transition metal cations in the gas phase has been widely studied over the past years [5–7]. The purpose of such studies, employing highly sensitive mass spectrometry, is to understand the fundamental chemical interactions in great detail. This is facilitated by the isolated nature of the reactions, which allows for the probing of intrinsic molecular interactions in full detail without being obscured by solvent interactions, substrates, or ensemble effects. Moreover, the limited system size allows for computational treatments at a highly accurate level of theory.

Only five third-row transition metal cations activate methane at room temperature, namely Ta^+, W^+, Os^+, Ir^+ and Pt^+ [8–15]. Of the first- and second-row transition metal cations, only Zr^+ and Nb^+ have been shown capable of activating methane at room temperature, despite these reactions being mildly endothermic [13,16–18]. The non-reactivity of other metals at room temperature does not mean they will not be active at higher temperatures; given enough input energy, the reaction of any ion with methane has been shown to lead to a rich activation chemistry [7]. It is therefore of interest to study the chemistry of metal ions with methane beyond the first activation step to understand the potential pathways that could play a role under industrial conditions above room temperature.

In a recent study, we reacted Pt^+ ions with multiple methane molecules in a room temperature ion trap at pressures up to 8×10^{-4} mbar, leading to sequential dehydrogenation reactions and the formation of $Pt(C_2H_4)_{1,2}^+$ complexes [19]. This observation contrasted with earlier work in our group where, in the relatively high-pressure environment of a molecular beam, dehydrogenation of the second methane molecule was kinetically hindered leading to the formation of a $Pt(CH_3)_2^+$ product [20]. Clearly, the lower-pressure conditions of the ion trap prevented efficient thermalization and opened access to the reactive potential energy surface well beyond the first activation step made accessible by the undissipated energies from the sequential adsorption of methane molecules.

In this work, we study the sequential adsorption of methane molecules onto the Ru^+ ion. Ruthenium was selected because, like the active osmium, it belongs to group 8 of the periodic table, and because ruthenium is a FTS catalyst [2]. Computationally, the products formed

☆ In celebration of Mary T. Rodger's 60th birthday and recognizing her many contributions to ion chemistry and spectroscopy.

* Corresponding author.
E-mail address: joost.bakker@ru.nl (J.M. Bakker).

https://doi.org/10.1016/j.ijms.2023.117165
Received 11 September 2023; Received in revised form 17 October 2023; Accepted 18 October 2023
Available online 19 October 2023

in the reaction between methane and Ru^+ have been studied extensively. Liu et al. reported that the $Ru(CH_4)^+$ adduct was lowest in energy, but also identified the $HRuCH_3^+$, $(H)_2RuCH_2^+$, $(H_2)RuCH_2^+$ and $RuCH_2^+ + H_2$ intermediates and reaction products on the doublet and quartet spin surfaces [21]. Later computational studies by Armentrout and Chen reproduced these results but added the $(H_2)HRuCH^+$ and $HRuCH^+ + H_2$ species on the doublet surface [15]. The stability of the $Ru(CH_4)^+$ adduct is consistent with experiments by Shayesteh and Böhme, who reacted methane with Ru^+ at room temperature in a helium buffer gas at a pressure of 0.47 mbar [13], significantly higher than in the current experiments. They only observed $[Ru,C,4H]^+$ and $[Ru,2C,8H]^+$, where the bracket notation implies no knowledge regarding the structure can be inferred from these mass spectrometry experiments. The dehydrogenation reaction $Ru^+ + CH_4 \rightarrow RuCH_2^+ + H_2$ was previously found to be endothermic by 1.17 ± 0.05 eV by guided ion beam tandem mass spectrometry (GIBMS) experiments, and the adsorption energy of the first methane molecule was calculated to be 0.78 eV [15]. The formation of $[Ru,C,2H]^+$ using different precursors has been reported: it can be formed in an endothermic (by 0.35 ± 0.05 eV) reaction of Ru^+ with cyclopropane (c-C_3H_6) [22] and in an exothermic (by 0.20 ± 0.05 eV) reaction of Ru^+ with oxirane (ethylene oxide, c-C_2H_4O) [23]. In a forthcoming publication, we will report on the spectroscopic characterization of $[Ru,C,2H]^+$ generated using the latter reaction. Here, we focus on reaction products of Ru^+ with multiple molecules of methane. If multiple molecules adsorb and the associated energy gain is not dissipated, dehydrogenation of methane may become a plausible reaction channel giving access to further reactions, such as the formation of C2 products. To complement these reactions with methane, we also investigate the reaction of Ru^+ with c-C_3H_6, but not with oxirane because of the larger energy release in the latter reaction, as well as the more complex product distribution. Armentrout and Chen found that reactions between c-C_3H_6 and Ru^+ under single collision conditions yielded only $[Ru,3C,4H]^+ + H_2$ and $[Ru,2C,2H]^+ + CH_4$ products at low reaction energies [22]. The only other low energy process observed was the already mentioned endothermic formation of $[Ru,C,2H]^+ + H_2$.

Here, we examine the products of Ru^+ with methane and c-C_3H_6 using a combination of Fourier transform ion cyclotron resonance (FTICR) mass spectrometry and IR multiple photon dissociation (IRMPD) spectroscopy. The combination of mass spectrometry and IR spectroscopy has been successful in characterizing the structures of reaction products of methane with ions of several elements, of which a review was recently published [24]. With mass spectrometry, we can identify the elemental composition of the products formed, and we spectroscopically characterize selected ions formed using the Free-Electron Laser for IntraCavity Experiments (FELICE) at the Free-Electron Lasers for Infrared eXperiments (FELIX) Laboratory. The IR spectra are interpreted using density functional theory (DFT) computed spectra of potential product structures. Theory is also used to examine the formation and fragmentation thermochemistry and mechanisms.

2. Methods

2.1. Experimental

Ruthenium cations were produced in a laser vaporization source as described elsewhere [25,26]. After production, the ions were cooled in an adiabatic expansion in He gas and transferred via a radio-frequency (rf) quadrupole mass filter in guidance mode to the room temperature quadrupole ion trap. Here, the ions were trapped in a bath of gas admitted via a leak valve and reacted with methane or c-C_3H_6 let in via a second leak valve. In the experiments with c-C_3H_6, products were formed with an Ar bath gas at partial pressures of 7–9 × 10^{-4} mbar and c-C_3H_6 partial pressures of 2–9 × 10^{-6} mbar. The reactions with methane were inefficient and required high methane partial pressures of 5.0 × 10^{-4} to 1.5 × 10^{-3} mbar; the additional use of Ar was not beneficial in product formation and was abandoned to reduce strain on the vacuum system.

After accumulating ions for ~0.5 s in the ion trap, the voltage on the trap exit electrode was lowered, effectively expelling the ions from the trap. These were then transferred to the 7 T FTICR mass spectrometer integrated in the cavity of the IR free-electron laser FELICE via an electrostatic bending quadrupole and an rf guiding quadrupole [27,28]. Ions were captured in FTICR cell 4 after which unwanted species were ejected via a combination of single frequency and chirped rf excitation pulses [29]. Of the species of interest, the ^{101}Ru (17 %) and ^{102}Ru (32 %) isotopes were isolated and the other Ru isotopes were ejected to avoid mass overlap between precursor and fragment ions. After isolation, the ions were irradiated by tunable IR light in the 350 - 2100 cm^{-1} spectral range, after which all ions present in the FTICR cell were mass-analyzed. All experiments in this study were carried out by irradiating the ions with a single FELICE macropulse in FTICR cell 4, which lies 30 cm or almost 4 times the Rayleigh range from the FELICE focus. Part of the light of FELICE was coupled out of the cavity to calibrate the wavelength and to determine the intra-cavity laser pulse energy. Spectral bandwidths range from 0.7 % of the central frequency in the low-frequency region to 0.3 % in the high-frequency region. Typical intra-cavity macropulse energies were in the range of 0.1–0.2 J for frequencies below 700 cm^{-1} and 0.4–0.7 J above 700 cm^{-1}, leading to laser fluences between 0.3 and 8 J/cm^2.

Infrared multiple photon dissociation (IRMPD) spectra of the activation products are presented as the fragmentation yield:

$$Y_F(\nu) = \frac{1}{P(\nu)} \ln\left(\frac{I_p(\nu) + I_f(\nu)}{I_p(\nu)}\right)$$

where $P(\nu)$ is the intra-cavity laser pulse energy at wavenumber ν, $I_p(\nu)$ is the summed intensities of the precursor ions in the mass spectrum, and $I_f(\nu)$ is the summed intensities of all observed fragment ions, primary and secondary, which must all originate from the parent ion as all ions except the parent ion are ejected prior to IR irradiation. Because the fragmentation yield is considered a proxy for the (relative) IR absorption cross-section, it is presented as unitless throughout this contribution. Stated band frequencies are obtained after fitting Gaussian curves to the experimental IRMPD spectra.

2.2. Computational

Density functional theory (DFT) calculations were performed using the Gaussian16 software package [30]. Geometries were optimized using the hybrid B3LYP functional [31,32] and the def2-TZVPPD basis set, which have been used before to describe similar systems including transition metals and hydrocarbons [15,19,20,33–37]. This basis set includes a small-core effective core potential (ECP) for Ru and explicitly treats the 4s, 4p, 5s, and 4d core and valence electrons. To benchmark our methods, we calculated several bond dissociation energies: $D_0(H_2–CH_2)$ = 4.67 eV (experimentally 4.743 ± 0.001 eV), $D_0((H_2C)_2–CH_2)$ = 3.74 eV (3.948 ± 0.004 eV), $D_0(Ru^+–CH_2)$ = 3.73 eV (3.57 ± 0.05 eV), $D_0(Ru^+–C_3H_4)$ = 2.57 eV (2.24 ± 0.12 eV) and $D_0(Ru^+–C_2H_2)$ = 2.34 eV (1.98 ± 0.18 eV) [22,23,38]. The theoretical and experimental values are relatively close together and therefore we assume that our method provides reasonable results. Trial structures were optimized on the doublet, quartet, and sextet spin surfaces. Vibrational frequencies were calculated in the harmonic approximation for comparison to the experiments, but also to ascertain that true minima were found for the reaction products and intermediates. Transition states (TSs) were ensured to be first-order saddle points that connect the corresponding intermediates on the potential energy surface (PES). All energies reported in this work were zero-point energy corrected using unscaled harmonic frequencies, whereas calculated spectra were corrected with a frequency scaling factor of 0.97 to compensate for anharmonicity and potential red shifts of vibrational bands resulting

from the IRMPD excitation mechanism.

To account for the potential broadening of the vibrational bands resulting from the underlying rotational envelope, rovibrational transitions were simulated using Prof. L. Meerts' homebuilt software package [39]. To do so, the rotational Hamiltonians for pure *a*-, *b*-, or *c*-type transitions were diagonalized yielding the frequencies and intensities of individual rovibrational transitions, which were weighted by a room temperature Boltzmann factor, combined with the calculated vibrational frequencies and intensities, and convoluted using a 0.9 % FWHM Gaussian function.

The calculations conducted herein do not include explicit consideration of spin-orbit interactions. For the ^{4}F ground electronic state of Ru^+, the spin-orbit splitting between the lowest J level (9/2) and the weighted mean of all spin-orbit levels is 0.175 eV [40]. Because most of the species considered in this work are simple adducts of this electronic state, it seems likely that the spin-orbit interactions in these complexes will be comparable to those for the bare ion, such that the calculated energetics will remain useful, certainly within the several tenths of an eV accuracy established above.

3. Results & discussion

3.1. Mass spectral analysis

Ruthenium has seven stable isotopes: ^{96}Ru (natural abundance 6 %), ^{98}Ru (2 %), ^{99}Ru (13 %), ^{100}Ru (13 %), ^{101}Ru (17 %), ^{102}Ru (32 %), and ^{104}Ru (19 %). The five heaviest isotopes are clearly present in the mass spectra shown in Fig. 1. They are presented on a mass scale relative to the most abundant ^{102}Ru isotope, facilitating identification of ligand products. The lightest product of the reaction between methane and Ru^+ observed in our room temperature ion trap is $[Ru,2C,4H]^+$ (+28 Da). This product could be formed via the sequential dehydrogenation of two methane molecules by the Ru^+ ion via the reaction $Ru^+ + 2\ CH_4 \rightarrow [Ru,2C,4H]^+ + 2H_2$. The other abundant reaction product observed is $[Ru,4C,6H]^+$ (+54 Da), which is presumably formed via $Ru^+ + 4\ CH_4 \rightarrow [Ru,4C,6H]^+ + 5H_2$. Both products are clearly visible in Fig. 1a, while ligands with one or three carbon atoms are not observed. Besides these major mass peaks, we observe smaller amounts of $[Ru,3C,O,4H]^+$ and $[Ru,4C,8H]^+$ (both +56 Da and resolved by the high resolution of the FTICR), $[Ru,2C,2O,4H]^+$ (+60 Da), and $[Ru,4C,O,6H]^+$ (+70 Da). All encountered reaction products are stated in Table 1. All species

Table 1
Observed products for the reaction of Ru^+ with methane or cyclopropane with possible loss channels. ΔM is the difference between product mass and the mass of Ru.

Reactants	Product ion	ΔM	Potential loss channels
$Ru^+ + 2\ CH_4$	$[Ru,2C,4H]^+$	28	$2H_2$
$Ru^+ + 2\ CH_4 + 2H_2O$	$[Ru,2C,2O,4H]^+$	60	$4H_2$
$Ru^+ + 3\ CH_4 + H_2O$	$[Ru,3C,O,4H]^+$	56	$5H_2$
$Ru^+ + 4\ CH_4$	$[Ru,4C,6H]^+$	54	$5H_2$
	$[Ru,4C,8H]^+$	56	$4H_2$
$Ru^+ + 4\ CH_4 + H_2O$	$[Ru,4C,O,6H]^+$	70	$6H_2$
$Ru^+ + c\text{-}C_3H_6$	$[Ru,3C,4H]^+$	40	H_2
	$[Ru,2C,2H]^+$	26	CH_4
	RuC^+	12	$C_2H_4 + H_2$ or C_2H_6
$Ru^+ + 2\ c\text{-}C_3H_6$	$[Ru,4C,6H]^+$	54	$C_2H_4 + H_2$ or C_2H_6
	$[Ru,5C,5H]^+$	65	$CH_3^\bullet + 2H_2$ or $CH_4 + H^\bullet + H_2$
	$[Ru,5C,6H]^+$	66	$CH_4 + H_2$
	$[Ru,6C,6H]^+$	78	$3H_2$

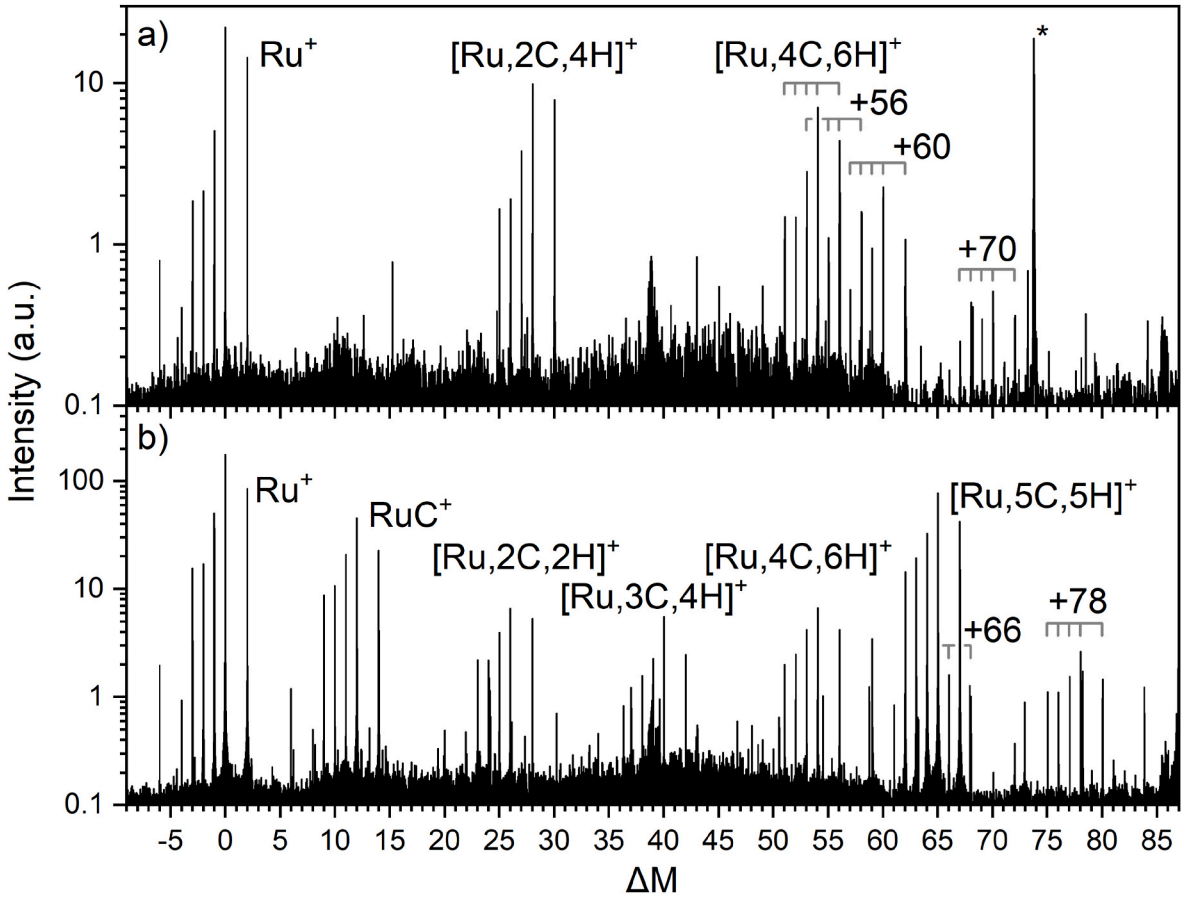

Fig. 1. Product mass distributions of the reaction between Ru^+ with a) methane and b) cyclopropane. ΔM is defined as the *m/z* value relative to the mass of ^{102}Ru, the most abundant Ru isotope. The asterisk (*) indicates an electronic artefact.

containing oxygen are likely the result from water contamination in the inlet system. $[Ru,4C,8H]^+$ is a very interesting product but has an intensity that is too low for IR characterization. Most other peaks, for example that at $\Delta M = 74$, are believed to be artifacts resulting from pickup of electrical noise because they do not show the characteristic isotopic pattern of ruthenium and the exact masses do not match any potentially produced molecule.

The ion distribution resulting from the reaction between *c*-C_3H_6 and Ru^+ is much richer, as shown in Fig. 1b. A single dehydrogenation of *c*-C_3H_6 likely forms $[Ru,3C,4H]^+$ via the reaction $Ru^+ + c\text{-}C_3H_6 \rightarrow [Ru,3C,4H]^+ + H_2$, whereas the $[Ru,2C,2H]^+$ product could be formed via loss of a methane molecule from *c*-C_3H_6 in the reaction $Ru^+ + c\text{-}C_3H_6 \rightarrow [Ru,2C,2H]^+ + CH_4$. These species were both found to be formed exothermically in the reaction between *c*-C_3H_6 and Ru^+ using GIBMS [22]. Another very abundant reaction product is $[Ru,5C,5H]^+$, which requires reaction with two cyclopropane molecules and the loss of a species with an odd number of hydrogen atoms. An example would be the reaction $Ru^+ + 2\ c\text{-}C_3H_6 \rightarrow [Ru,5C,5H]^+ + CH_3^{\bullet} + 2H_2$, where $CH_3^{\bullet}$ is a methyl radical. Another reaction pathway could involve loss of atomic hydrogen. We assume that the $[Ru,4C,6H]^+$ species formed here is similar to that produced in the methane case, but this was not checked explicitly. We also observed small amounts of $[Ru,5C,6H]^+$ (+66 Da) and $[Ru,6C,6H]^+$ (+78 Da) but did not spectroscopically characterize these species because their abundances were too low. The prominent RuC^+ product is not investigated in this study but its formation along with C_2H_6 by reaction of Ru^+ with *c*-C_3H_6 is endothermic by 0.50 ± 0.08 eV according to GIBMS experiments [15,22,23]. Its intensity suggests it is not a secondary process, implying that some additional source of energy is available to the reactions under the experimental conditions used here. This could include incomplete quenching of electronically excited Ru^+ states formed in the ablation process or excess kinetic energy when injecting the Ru^+ ions into the ion trap.

3.2. IR spectroscopy of $[Ru,2C,4H]^+$

IR irradiation of the isolated mass channels $m/z = 129$ and 130, corresponding to the ^{101}Ru and ^{102}Ru isotopes of $[Ru,2C,4H]^+$, results in two fragments (Fig. S1). One fragment is observed at mass channels $m/z = 127$ and 128 and corresponds to the dehydrogenation product $[Ru,2C,2H]^+$. The other fragment observed is the bare Ru^+ ion. From the wavelength dependent ion intensities shown in Fig. S1, it can be concluded that $[Ru,2C,2H]^+$ is the primary fragment. Thus, dehydrogenation is the most important loss channel of $[Ru,2C,4H]^+$. The Ru^+ fragment is only visible on the low frequency side of one of the experimental bands around 1400 cm^{-1}. Because the $[Ru,2C,4H]^+$ spectrum overlaps with an IR band observed at 1394 cm^{-1} for the $[Ru,2C,2H]^+$ species (see section 5, Fig. 5 and S7), we believe that the Ru^+ fragment is a secondary loss channel, only formed when $[Ru,2C,4H]^+$ loses dihydrogen to form $[Ru,2C,2H]^+$, which then accepts IR photons to eliminate C_2H_2.

The IRMPD spectrum of $[Ru,2C,4H]^+$ recorded using both fragments is shown in Fig. 2a. Strong bands are observed at 978 and 1438 cm^{-1}, of which the latter is broader and where, in the tail to the red, a weak band at 1258 cm^{-1} can be identified. A final band of medium intensity is observed at 1942 cm^{-1}.

One of the possible product structures for the $[Ru,2C,4H]^+$ complex could contain an ethene molecule. The free ethene molecule has three IR active bands in the observed region: a weak one at 826 cm^{-1} and stronger bands at 949 and 1444 cm^{-1}, associated with the rocking, in-phase wagging, and scissoring motions of the two CH_2 groups, respectively [41]. The latter two are very close to the 978 and 1438 cm^{-1} bands observed in the experimental IRMPD spectrum of $[Ru,2C,4H]^+$, suggesting that the product found could indeed contain an ethene ligand. Notably, because complexation with Ru^+ breaks the D_{2h} symmetry of free ethene, IR forbidden bands in free ethene, such as the out-of-phase CH_2 wagging mode at 943 cm^{-1} or the C═C stretch at

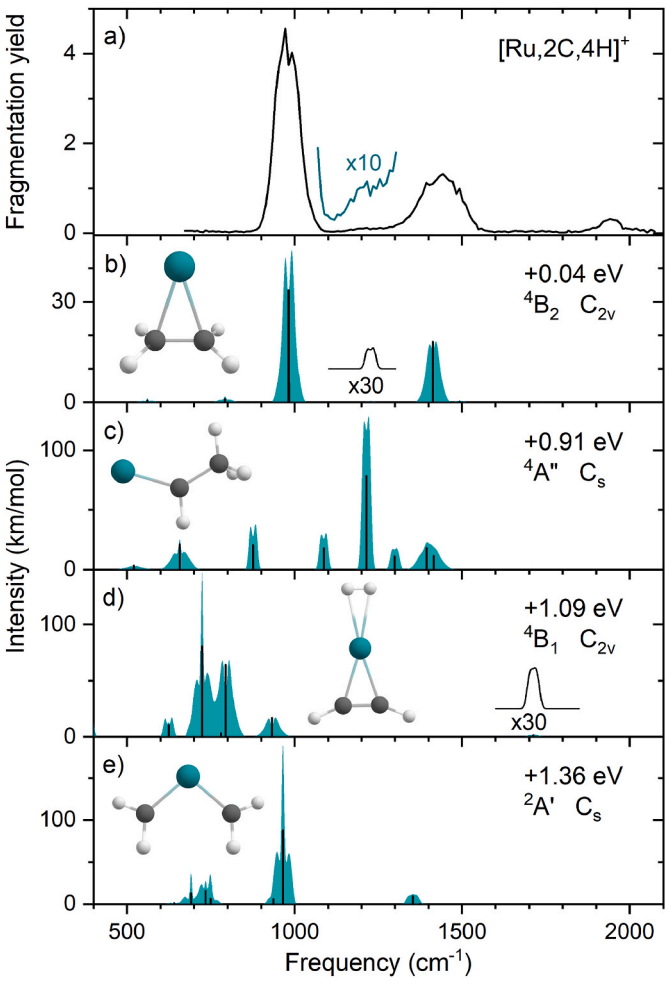

Fig. 2. a) Experimental IRMPD spectrum of $[Ru,2C,4H]^+$. b–e) Calculated IR spectra of $[Ru,2C,4H]^+$ isomers including rovibrational simulations at room temperature. Simulations are accompanied by molecular structures, electronic states, point groups, and theoretical energies relative to the $Ru^+ + 2\ CH_4$ reactants.

1623 cm^{-1} could gain IR intensity.

To compare the observed IRMPD spectrum with calculated spectra of potential product structures, eight trial structures for the $[Ru,2C,4H]^+$ species were optimized. Calculated IR spectra of selected $[Ru,2C,4H]^+$ isomers are shown in Fig. 2b–e and the rest in Fig. S2. The lowest energy isomer, $Ru(C_2H_4)^+$ with a $^4B_2$ electronic state, contains an ethene ligand coordinated to Ru^+, and has an energy 0.04 eV above the energy of the reactants assuming the formation of two H_2 product molecules. The ethene binds via the carbon atoms in an η^2 configuration to the Ru^+ ion. There is a low-lying $^4B_1$ state lying only 0.08 eV higher in energy with a very similar spectrum (not shown). This state differs only in the occupation of the non-bonding δ-like orbitals ($5d^2_{x2\text{-}y2}\ 5d^1_{xy}$ for $^4B_2$ versus $5d^1_{x2\text{-}y2}\ 5d^2_{xy}$ for $^4B_1$). The low-spin $^2A_2$ state of $Ru(C_2H_4)^+$ has a very similar spectrum (Fig. S2b), but this state is 0.51 eV higher in energy compared to the $^4B_2$ state. Other geometries considered are $RuCHCH_3^+$, $(H_2)Ru(C_2H_2)^+$, $Ru(CH_2)_2^+$, $(H)_2Ru(C_2H_2)^+$, $HCRuCH_3^+$, and two isomeric structures of $HRu(CHCH_2)^+$, but these geometries are all calculated to be at least 0.9 eV above the energy of the reactants. The energetics and electronic states of all isomers presented in this manuscript are summarized in Table S1.

Comparison of the experimental and calculated spectra confirms the similarity between the experimental spectrum and that of free ethene: all experimental bands except one can be explained by the calculated spectrum for the $Ru(C_2H_4)^+$ ($^4B_2$) (or possibly $^4B_1$) structure, where an

ethene ligand binds to ground state Ru^+ (^4F). The experimental band at 978 cm^{-1} matches the out-of-phase and in-phase CH_2 wagging vibrations calculated for $Ru(C_2H_4)^+$ at 982 and 983 cm^{-1} (intensities of 34 and 6 km/mol, respectively), that have blue shifted from their frequencies of 943 and 949 cm^{-1} in free ethene. The experimental band at 1438 cm^{-1} matches the out-of-phase CH_2 scissoring vibration calculated at 1413 cm^{-1} (free ethene: 1444 cm^{-1}). Even the experimentally very weak band at 1258 cm^{-1} can be explained by a mode having both symmetric CH_2 scissoring and C–C stretch character, calculated at 1226 cm^{-1}. The CH_2 rocking vibration is calculated at 792 cm^{-1} but is relatively weak at 1 km/mol, and not observed. Simultaneously, the comparison allows us to exclude all alternative geometries. The absence of experimental bands between 700 and 900 cm^{-1} excludes the presence of an ethyne ligand, whereas the intensity ratio of the experimental bands rules out the $RuCHCH_3^+$ structure. The absence of experimental bands around 750 cm^{-1} together with the absence of a calculated band between 1000 and 1300 cm^{-1} argues against $Ru(CH_2)_2^+$, as do the energetics. The lack of experimental bands around or beneath 900 cm^{-1} argues against either $HRu(CHCH_2)^+$ species. The only experimental band for which $Ru(C_2H_4)^+$ fundamental vibrations offer no explanation is the 1942 cm^{-1} band. Likely, this band originates from an overtone of the strongest experimental band at 978 cm^{-1} or from a combination band. An anharmonic calculation of $^4B_2$ $Ru(C_2H_4)^+$ finds overtones of the wagging modes at 1994 cm^{-1} (0.4 km/mol, antisymmetric) and 2002 cm^{-1} (0.8 km/mol, symmetric), and combination bands of the antisymmetric wagging mode with its symmetric counterpart at 1997 cm^{-1} (3.4 km/mol), and with the IR-inactive antisymmetric CH_2 twisting mode at 1904 cm^{-1} (2.3 km/mol).

The ethene ligand in the assigned $Ru(C_2H_4)^+$ ($^4B_2$) structure is mildly activated. The calculated C–C distance in free ethene of 1.325 Å is significantly elongated to 1.390 Å in $Ru(C_2H_4)^+$. The C–H distances are barely affected: calculated as 1.083 Å in free ethene and 1.086 Å for $Ru(C_2H_4)^+$. The ethene ligand is distorted from planar by the Ru^+ ion with the hydrogen atoms on average pushed away from a planar ligand by 0.143 Å, away from the Ru^+ ion. The Ru^+ ion lies 2.069 Å above the center of the C–C bond and both Ru^+–C distances are 2.182 Å. Charge transfer was assessed using a Mulliken population analysis, based on the electron density in molecular orbitals, which predicts that the Ru atom in $Ru(C_2H_4)^+$ holds a charge of +0.593 e with the rest of the charge distributed over the ethene ligand [42]. An atomic polar tensor (APT) analysis, based on a changing dipole moment, yields +0.677 e on the Ru^+ ion [43]. Both values indicate that the ethene ligand donates electron density to the Ru^+ ion, most likely originating from the C=C π bond. In contrast, a natural bond orbital analysis (NBO) [44,45] finds the charge on Ru^+ is +0.975 e, such that there is minimal electron density shifted from the ethene ligand.

With the assignment of the spectrum in hand, we can evaluate the energetics of the decompositions observed. Dehydrogenation of $Ru(C_2H_4)^+$ to form $Ru(C_2H_2)^+$ is calculated to require at least 1.46 eV. This product can then undergo further IR absorption, leading to loss of the acetylene ligand and formation of Ru^+. This conclusion is consistent with calculated energies that indicate direct ethene loss from $[Ru,2C,4H]^+$ requires 2.00 eV (>1.34 eV from experiment) [22].

3.3. IR spectroscopy of $[Ru,4C,6H]^+$

IR irradiation of the isolated mass channels m/z = 155 and 156 of $[Ru,4C,6H]^+$ results in two fragments (Fig. S3). One fragment is observed at the m/z = 153 and 154 mass channels of $[Ru,4C,4H]^+$ corresponding to dehydrogenation and the other fragment is formed by the m/z = 127 and 128 mass channels of $[Ru,2C,2H]^+$, either via direct C_2H_4 loss or loss of $C_2H_2 + H_2$. The weaker IR bands of $[Ru,4C,6H]^+$ are only observed in the $[Ru,4C,4H]^+$ fragment channel as shown in Fig. S3, whereas formation of $[Ru,2C,2H]^+$ is only observed in the main bands at 900 and 1400 cm^{-1}. These observations indicate that dehydrogenation is presumably the dominant fragmentation channel. This is particularly clear at 900 cm^{-1}, where the $[Ru,4C,4H]^+$ channel has a volcano-like structure centered around a sharper peaked band in the $[Ru,2C,2H]^+$ channel, suggesting $[Ru,2C,2H]^+$ is only formed at the most intense part of the $[Ru,4C,6H]^+$ band and likely requires the formation of the $[Ru,4C,4H]^+$ fragment and probable further IR absorption by the fragment ion.

The IRMPD spectrum of $[Ru,4C,6H]^+$ is constructed using both fragments and is shown in Fig. 3a. It is dominated by two strong bands at 950 and 1386 cm^{-1}, with the latter showing a secondary maximum at 1471 cm^{-1}. Three weak bands are observed at 719, 1044, and 1918 cm^{-1}.

Computationally, twelve trial structures for the $[Ru,4C,6H]^+$ species were evaluated. Calculated IR spectra of four of these are shown in Fig. 3b–e and the rest in Fig. S4. The lowest energy isomer found has a *cis*-1,3-butadiene ligand, where the four carbon atoms lie in one plane with close to 120° bond angles. The ligand is bound in a η^4 fashion, where all four carbon atoms are coordinated to Ru^+, which is located above the half-ring. The structure is found on the doublet surface, with the quartet equivalent lying 0.83 eV higher in energy (Fig. S4c). Other geometries for $[Ru,4C,6H]^+$ include $Ru(C(CH_2)_3)^+$, $HRu(c\text{-}C_4H_5)^+$, $(C_2H_4)Ru(C_2H_2)^+$, $(C_2H_4)RuCCH_2^+$, and $Ru(c\text{-}C_4H_6)^+$. Except for the doublet spin complex with *trans*-1,3-butadiene, which has a very similar spectrum to that of the *cis*-structure (Fig. S4b) and lies 0.32 eV higher in energy, all other geometries are at least 0.7 eV higher in energy than Ru

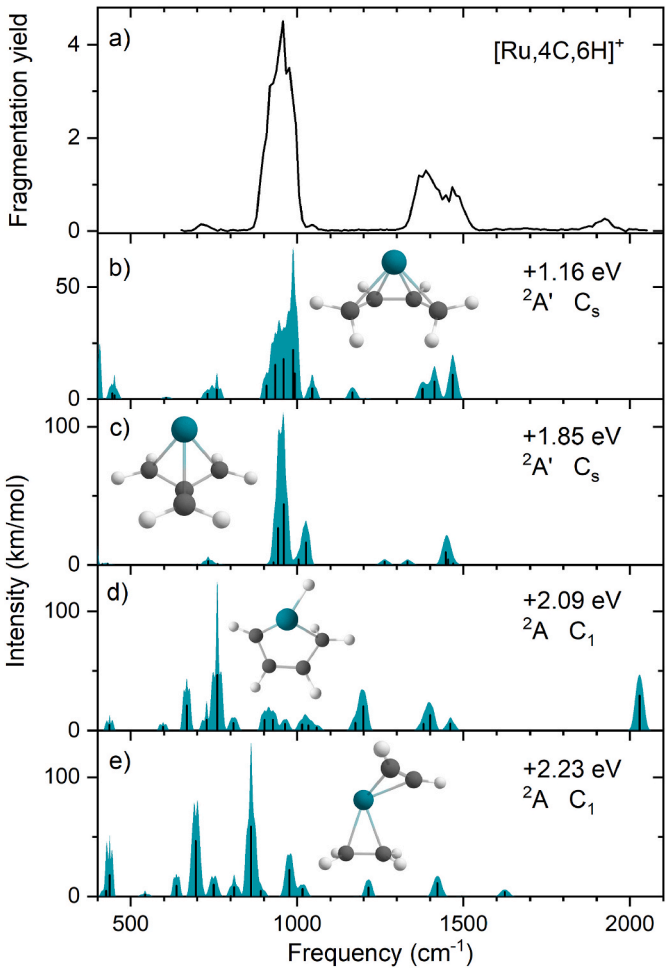

Fig. 3. a) Experimental IRMPD spectrum of $[Ru,4C,6H]^+$. b–e) Calculated IR spectra of $[Ru,4C,6H]^+$ isomers including rovibrational simulations at room temperature. Simulations are accompanied by molecular structures, electronic states, point groups, and theoretical energies relative to the Ru^+ + 4 CH_4 reactants.

(*cis*-1,3-butadiene)$^+$.

Comparison of the experimental IRMPD spectrum of [Ru,4C,6H]$^+$ with the calculated IR spectra allows discarding the HRu(*c*-C_4H_5)$^+$ and (C_2H_4)Ru(C_2H_2)$^+$ geometries as possible candidates because these do not have their most intense vibrations at frequencies close to the strong bands at 950 and 1386 cm^{-1}. The match with the Ru(*cis*-1,3-butadiene)$^+$ geometry is better compared to Ru(*trans*-1,3-butadiene)$^+$ (Fig. S4b) and Ru(C(CH_2)$_3$)$^+$ geometries because of the distribution of bands around 1400 cm^{-1}. This is also true for the quartet spin state of Ru(*cis*-1,3-butadiene)$^+$ where Ru$^+$ binds to only two carbon atoms. The only experimental band that cannot be assigned to a fundamental vibration predicted for Ru(*cis*-1,3-butadiene)$^+$ is the weak band at 1918 cm^{-1}, which we speculate is an overtone of the intense experimental band at 950 cm^{-1}. The weak calculated band at 1166 cm^{-1} is not observed, but its calculated intensity of only 3 km/mol could explain this. On the basis of this favorable comparison and because it is the lowest energy structure found, we assign the IRMPD spectrum to Ru(*cis*-1,3-butadiene)$^+$ in the ^{2}A' state. The experimental band at 950 cm^{-1} is not well enough resolved in the current experiment to discern all individual computed bands, which are all C–H out-of-plane bending vibrations of the butadiene molecule. The experimental band at 1044 cm^{-1} corresponds to a calculated vibration at 1046 cm^{-1} with an intensity of 5 km/mol involving both in-plane and out-of-plane C–H motions. The experimental bands at 1386 and 1471 cm^{-1} correspond to skeletal deformations involving C–C stretches of the butadiene molecule and that at 719 cm^{-1} to the twisting of both terminal CH_2 groups, calculated at 731 (A″) and 759 (A′) cm^{-1}.

Free butadiene is close to planar and has terminal C=C bonds with a length calculated as 1.333 Å, with the middle C–C bond length being 1.468 Å. The butadiene ligand in Ru(η^4-*cis*-1,3-butadiene)$^+$ is distorted by the Ru$^+$ ion that is positioned centrally above the ligand plane, with calculated Ru–C bond lengths for terminal and middle carbon atoms almost identical at 2.106 and 2.115 Å, respectively. The two terminal C–C bonds have a length of 1.419 Å (+0.086 Å compared to free butadiene) and the middle C–C bond length is 1.431 Å (−0.037 Å). All bonds in the ligated *cis*-1,3-butadiene are thus relatively similar in length, which may indicate a strongly delocalized electron distribution in the carbon chain. The similar lengths of all three C–C bonds for a butadiene ligand was noted before by Grée et al. who found C–C bond lengths in (η^4-butadiene)Fe(CO)$_3$ between 1.404 Å and 1.424 Å for both the terminal and middle C–C bonds [46]. According to the Mulliken charge analysis, the Ru atom in Ru(*cis*-1,3-butadiene)$^+$ carries +0.400 e, whereas the APT charge analysis gives a value of +0.390 e, implying that the *cis*-1,3-butadiene ligand holds most of the positive charge. An NBO analysis indicates less but still substantial charge transfer with a charge on Ru of +0.714 e.

3.4. IR spectroscopy of [Ru,3C,4H]$^+$

IR irradiation of the isolated mass channels m/z = 141 and 142 of [Ru,3C,4H]$^+$ results in two fragments (Fig. S5). The fragment observed at the mass channels m/z = 113 and 114 of RuC$^+$ likely corresponds to the loss of ethene; a second fragment is the bare Ru$^+$ ion at m/z = 101 and 102. Both RuC$^+$ and Ru$^+$ fragments are approximately equally intense as shown in Fig. S5, suggesting that loss of C_2H_4 and C_3H_4 are competing channels with similar fragmentation barriers.

The resulting IRMPD spectrum is recorded using two IR laser settings as shown in Fig. 4a. A total of six bands can be seen in this spectrum: two relatively sharp bands at 667 and 763 cm^{-1} that partially overlap, a strong, structured band peaking at 1346 cm^{-1} with a shoulder on the blue side at 1504 cm^{-1}, a broad band around 1000 cm^{-1} and a weaker band at 1787 cm^{-1}.

In the calculations, we found fifteen structures for which calculated IR spectra are shown in Fig. 4b–e and S6. In the lowest energy isomer found (quartet spin state), propyne is coordinated to Ru$^+$ via its C≡C triple bond and has an energy 1.38 eV below that of the Ru$^+$ + *c*-C_3H_6 reactants assuming concomitant H_2 formation. The analogous doublet structure lies 0.53 eV higher in energy and has a similar spectrum (Fig. S6d). Other geometries include Ru(propadiene)$^+$, other Ru(C_3H_4)$^+$ isomers, HRu(C_3H_3)$^+$ isomers, (C_2H_2)RuCH_2^+, CRu(C_2H_4)$^+$, H_2CRuCCH_2^+, and HCRuCHCH_2^+, which are all at least 0.3 eV higher in energy.

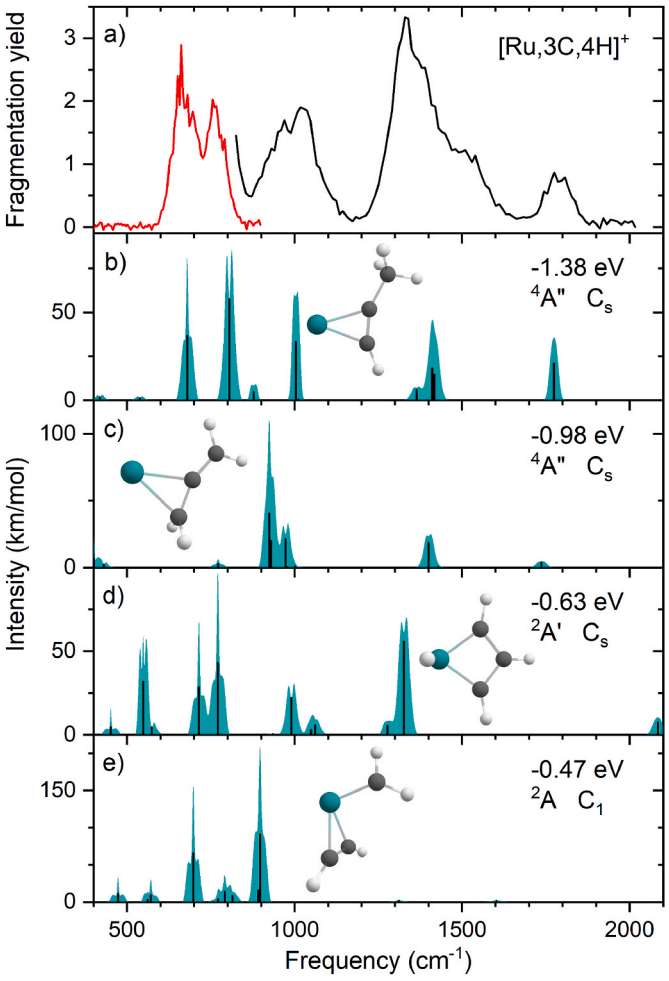

Fig. 4. a) Experimental IRMPD spectrum of [Ru,3C,4H]$^+$. The red and black traces were recorded using different FEL settings. b–e) Calculated IR spectra of [Ru,3C,4H]$^+$ isomers including rovibrational simulations at room temperature. Simulations are accompanied by molecular structures, electronic states, point groups, and theoretical energies relative to the Ru$^+$ + *c*-C_3H_6 reactants.

In contrast to the comparisons with calculated spectra discussed above, the computations for the current candidate structures predict IR activity above 1500 cm^{-1} allowing the inclusion of the 1787 cm^{-1} band in the comparison. Such a comparison favors the Ru(propyne)$^+$ (^{4}A″) lowest energy structure, with five bands matching the main experimental bands relatively well, although the in-plane vibration of the hydrogen atom bonded to the C≡C triple bond calculated at 805 cm^{-1} has a somewhat different frequency than the 763 cm^{-1} experimental band. The 1787 cm^{-1} experimental band matches the C≡C stretch mode calculated at 1774 cm^{-1}, although its observed intensity appears on the low side. The Ru(propadiene)$^+$ and (C_2H_2)RuCH_2^+ species clearly do not reproduce all bands observed in the experiment, allowing us to discard them as the dominant product observed. The HRu(CHCHCH)$^+$ spectrum shown in Fig. 4d offers a serious alternative with matching bands in the 600–1500 cm^{-1} spectral range, but we exclude it because there is no band observed near 550 cm^{-1}. Thus, we assign the spectrum to Ru(propyne)$^+$ (^{4}A″), the lowest energy structure located, although contributions from Ru(propadiene)$^+$ cannot be eliminated. Here, the

experimental band centered around 1000 cm^{-1} is assigned to the out-of-plane bending mode of the CH_3 group of propyne, calculated at 1004 cm^{-1}. The experimental band at 667 cm^{-1} is assigned to the out-of-plane vibration of the hydrogen atom bonded to the terminal carbon of the C≡C triple bond calculated at 680 cm^{-1}. The three calculated modes around 1400 cm^{-1} correspond to vibrations of the CH_3 group, which are not individually observed in the IRMPD spectrum as the experimental resolution is too low. The main discrepancy between the experimental and Ru(propyne)$^+$ ($^4A''$) predicted spectrum is the shoulder at 1504 cm^{-1}. This could potentially originate from a combination or overtone band of the intense bands at 667 and 763 cm^{-1}.

In free propyne, the carbon backbone is linear with C≡C and C–C bond lengths calculated to be 1.200 and 1.454 Å, respectively. The propyne ligand in Ru(η^2-propyne)$^+$ is distorted, with a CCC angle of 156° and the C≡C and C–C bonds elongated to 1.275 Å (+0.075 Å) and 1.469 Å (+0.015 Å), respectively. The Ru–C bond lengths are 1.991 Å for the terminal carbon and 2.033 Å for the middle carbon atom, so the Ru^+ ion coordinates close to the middle of the C≡C bond, which it weakens considerably, exemplified by the reduction of the C≡C stretch vibration from 2142 cm^{-1} in free propyne to 1744 cm^{-1} in the complex [41]. One of the C≡C π bonds points directly at Ru and has A′ symmetry, while the other π bond has A″ symmetry. These different binding possibilities allow several Ru orbitals to overlap with either of the C≡C π bonds, thereby leading to a strong bond between Ru^+ and the ligand. Mulliken, APT, and NBO charge analyses attribute quite different charges to the Ru atom: +0.366 e versus +0.724 e versus +0.919 e, respectively. All imply electron donation from propyne to Ru^+ but they clearly differ in the extent of this donation.

Experimentally, $D_0(Ru^+–C_3H_4) = 2.24 \pm 0.12$ eV [22], and the loss of ethene from $[Ru,3C,4H]^+$ to form RuC^+ was determined to be endothermic by 2.82 ± 0.14 eV [15,22,23]. The former bond energy is somewhat lower than our calculated value of 2.57 eV for the loss of propyne, whereas the latter is somewhat higher than our calculated value of 2.54 eV. The comparable theoretical values are in good agreement with the experimental observation of two almost equal intensity fragmentation channels.

3.5. IR spectroscopy of $[Ru,2C,2H]^+$

IR irradiation of the isolated mass channels m/z = 127 and 128 of $[Ru,2C,2H]^+$ results in formation of the bare Ru^+ ion (Fig. S7). The IRMPD spectrum of $[Ru,2C,2H]^+$ in Fig. 5a is relatively simple with one strong main band peaking just below 750 cm^{-1}, which has a side peak at 692 cm^{-1}, and a weaker band at 1394 cm^{-1}.

An obvious candidate ligand in the $[Ru,2C,2H]^+$ complex is ethyne, C_2H_2 (acetylene). Free ethyne is linear and has three modes in the region observed, namely the concerted CH bending modes at 730 cm^{-1} (in-phase, π_u symmetry), its π_g out-of-phase counterpart at 612 cm^{-1}, and the C–C stretch vibration at 1974 cm^{-1} [41]. The frequencies of both bending modes are quite close to the main band in the experimental IRMPD spectrum.

The ethyne ligand is one of the five structures evaluated in the computations shown in Fig. 5b–e and S8. Formed along with CH_4, Ru$(C_2H_2)^+$ ($^4B_1$) was found to be lowest in energy at 1.48 eV below that of the reactants. A $^4B_2$ state differing only in the δ-like orbital occupations lies another 0.17 eV higher in energy and has a similar spectrum (not shown). Other geometries considered include $RuCCH_2^+$, $CRuCH_2^+$, Ru$(CH)_2^+$, and $HRuCCH^+$, but all are at least 0.5 eV higher in energy.

Upon comparison of the experimental spectrum to the calculated spectrum for the $^4B_1$ state of Ru$(C_2H_2)^+$, one immediately notes that there is no fundamental frequency predicted near 1394 cm^{-1}. The CH bending modes of free ethyne are doubly degenerate and split in the ruthenium complex to two in-plane bends (A_1 symmetry, 781 cm^{-1} and B_2, 829 cm^{-1}) and two out-of-plane bends (B_1, 721 cm^{-1} and A_2, 715 cm^{-1}) with the B symmetry modes being much more intense. The dyad band observed at 692/750 cm^{-1} could potentially be assigned to these

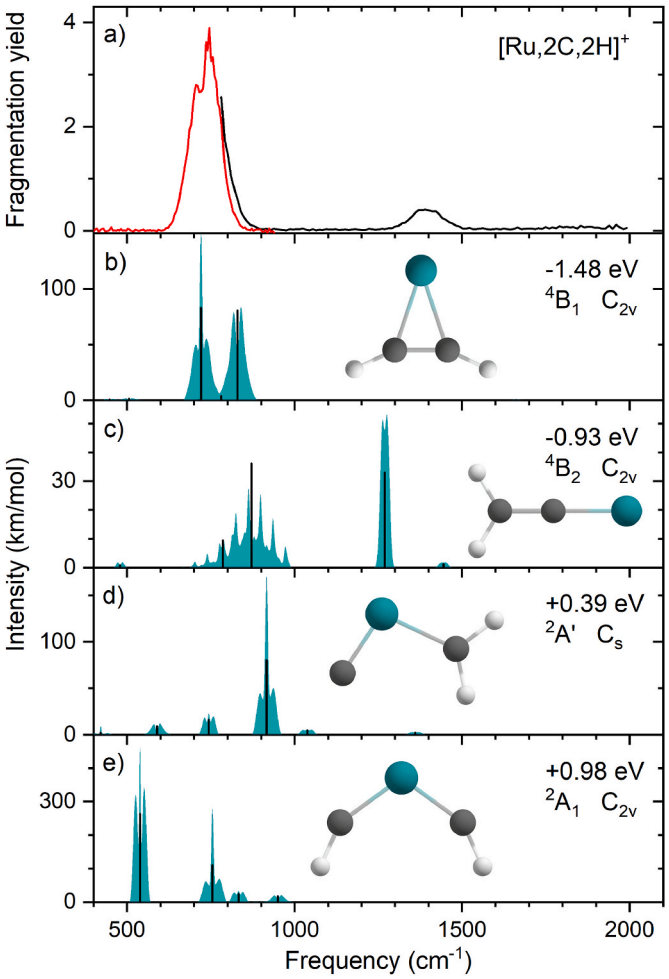

Fig. 5. a) Experimental IRMPD spectrum of $[Ru,2C,2H]^+$. The red and black traces were recorded using different FEL settings. b–e) Calculated IR spectra of $[Ru,2C,2H]^+$ isomers including rovibrational simulations at room temperature. Simulations are accompanied by molecular structures, electronic states, point groups, and theoretical energies relative to the Ru^+ + c-C_3H_6 reactants.

bands, presuming they have nearly merged in the IR excitation process, assisted by the presence of the weaker 781 cm^{-1} band in between. The $^4B_2$ state of Ru$(C_2H_2)^+$ has the intense B_1 mode at nearly the same position (720 cm^{-1}) as the $^4B_1$ state, whereas the B_2 mode is predicted slightly lower in frequency (808 cm^{-1}). The spectrum calculated for $RuCCH_2^+$ (panel 5c) has three bands at 786, 871, and 1269 cm^{-1}, of which the latter two are the most intense, although only the 1269 cm^{-1} band is an a-type transition resulting in a narrow rotational envelope. This spectrum does not match the experiment because the band at 871 cm^{-1} is even higher in frequency than the predicted bands for Ru$(C_2H_2)^+$. Moreover, the calculated band at 1269 cm^{-1} is not only predicted too low in frequency but is also far too intense to be assigned to the experimental 1394 cm^{-1} band. (Here, it can be recognized that the one-photon theoretical intensities and the multiple photon experimental intensities are not necessarily directly comparable, but the relative intensities of the two main bands of $RuCCH_2^+$ are strikingly different from the experimental intensities.) The spectra for $CRuCH_2^+$ and Ru$(CH)_2^+$ offer no better alternative. The Ru$(C_2H_2)^+$ ($^2B_1$) species (Fig. S8b) has bands predicted around 750 cm^{-1}, but their frequency differences are even larger than predicted for the $^4B_1$ state, and the energy of the doublet state is 0.59 eV higher than the quartet. Consequently, we assign the experimental spectrum to the $^4B_1$ state of Ru$(C_2H_2)^+$. The 1394 cm^{-1} band must then be attributed to an overtone of either of the two CH bending modes or to a combination band of the two, not unlike the

shoulder observed for $[Ru,3C,4H]^+$.

Ethyne in the $Ru(\eta^2\text{-}C_2H_2)^+$ ($^4B_1$) complex is distorted with CCH angles of 155° and calculated C≡C and C–H bond lengths are lengthened from 1.197 and 1.062 Å to 1.269 (+0.072) and 1.077 (+0.015) Å, respectively. The Ru–C distances in $Ru(C_2H_2)^+$ are both 2.010 Å. According to the Mulliken charge analysis, the Ru atom in $Ru(C_2H_2)^+$ ($^4B_1$) carries +0.507 e and according to the APT charge analysis Ru carries +0.790 e. Again, an NBO analysis finds little electron density is donated to Ru^+, which retains a charge of +0.967 e.

3.6. IR spectroscopy of $[Ru,5C,5H]^+$

IR irradiation of the isolated mass channels $m/z = 166$ and 167 of $[Ru,5C,5H]^+$ results in a total of five fragments (Fig. S9). The mass channels at $m/z = 140$ and 141 correspond to loss of C_2H_2 to form $[Ru,3C,3H]^+$, and mass channels $m/z = 138$ and 139 are $[Ru,3C,H]^+$ ions, which either correspond to loss of C_2H_4 or to dehydrogenation of $[Ru,3C,3H]^+$. Other fragments are $m/z = 127$ and 128 of $[Ru,2C,2H]^+$, $m/z = 113$ and 114 of RuC^+, and the bare Ru^+ ion at $m/z = 101$ and 102. $[Ru,3C,3H]^+$ and $[Ru,3C,H]^+$ are the most intense photofragments of $[Ru,5C,5H]^+$ as shown in Fig. S9. From the strong band at 860 cm^{-1}, where there is a volcano-like structure of the $[Ru,3C,3H]^+$ trace that is centered around the maximum of the $[Ru,3C,H]^+$ trace, it appears that $[Ru,3C,H]^+$ is a secondary fragment, formed by dehydrogenation of $[Ru,3C,3H]^+$. Less intense fragments are the bare Ru^+ ion, the RuC^+ ion, and $[Ru,2C,2H]^+$. These fragments have broader absorption bands around similar frequencies as $[Ru,3C,3H]^+$ and $[Ru,3C,H]^+$, except for $[Ru,2C,2H]^+$, which is most intense around 950 cm^{-1}. In particular, the width of the Ru^+ bands appears to suggest that this is a higher energy loss channel that is subject to power broadening.

The IRMPD spectrum of $[Ru,5C,5H]^+$ recorded using all five fragments is shown in Fig. 6a. It is arguably the best-resolved spectrum obtained here, dominated by an intense band at 860 cm^{-1}, with a moderately intense band at 408 cm^{-1}. Three other bands of lower intensity are observed at 979, 1374, and 1746 cm^{-1}. The red trace in Fig. 6a, which was recorded using different FELICE conditions, shows an additional broad absorption plateau around 785 cm^{-1}.

Three trial structures were computationally investigated for the $[Ru,5C,5H]^+$ species as shown in Fig. 6 and S10. The lowest energy isomer contains a cyclopentadienyl (*c*-C_5H_5) ligand with the Ru^+ ion centered above the ring, resulting in C_{5v} symmetry. On the singlet surface, this complex + CH_3 + $2H_2$ has an energy 1.71 eV below the energy of the Ru^+ + 2 *c*-C_3H_6 reactants. On the triplet and quintet spin surfaces, the system is subject to Jahn-Teller distortion leading to C_s structures; the energies of their formation remain exothermic by 0.81 and 0.30 eV, respectively. The other geometries considered are $(C_2H_2)Ru(CHCHCH)^+$ and $HCRu(C_2H_2)_2^+$, both of which are at least 2.4 eV above the ground structure and thus can only be formed in endothermic processes.

Comparison of the spectra in Fig. 6 leave little doubt that the experimental spectrum should be assigned to singlet $Ru(c\text{-}C_5H_5)^+$ ($^1A_1$), with the four main bands presenting excellent agreement with the experimental spectrum. Assignment to $(C_2H_2)Ru(CHCHCH)^+$ and $HCRu(C_2H_2)_2^+$ in any spin state can be spectrally ruled out and further, these are energetically unlikely. The spectral match is also clearly much better for the singlet cyclopentadienyl complex than for the triplet species, which does not reproduce the strong band at 408 cm^{-1}. This band is assigned to an overlap of the bending (hindered ligand rotation) and stretching mode of the Ru^+–(*c*-C_5H_5) bond, calculated at 402 and 415 cm^{-1}, respectively. The strong experimental band at 860 cm^{-1} is associated with the C_5H_5 umbrella mode calculated at 872 cm^{-1} (49 km/mol). Two more bands representing out-of-plane hydrogen bending vibrations are calculated at 880 cm^{-1}, both with a calculated intensity of 10 km/mol. The experimental band at 979 cm^{-1} matches with two vibrations at 985 cm^{-1} corresponding to hydrogen bending motions in the *c*-C_5H_5 plane, both with an intensity of 8 km/mol. The experimental band at 1374 cm^{-1} matches two in-plane ring deformation modes of the cyclopentadienyl ligand, both calculated at 1396 cm^{-1} and 13 km/mol intensity. Only the experimental band at 1746 cm^{-1} cannot be assigned to a fundamental vibration, but it lies at roughly twice the frequency of the strong experimental band at 860 cm^{-1}. Thus, we suspect that it is the overtone of the intense umbrella mode (calculated at 872 cm^{-1}), or of one of the out-of-plane CH bending vibrations both calculated at 880 cm^{-1}, or a combination band involving any of these. We also note that in one of the scans (red trace in Fig. 6a), we observe a weak plateau below 800 cm^{-1}. Inspection of the fragmentation products in Fig. S9, panel c shows that no $[Ru,3C,3H]^+$ are formed, suggesting this is not simply the onset of the intense band at 860 cm^{-1}, but an indication of a small population of one of the minor alternative isomers, which have absorption bands just below 800 cm^{-1}.

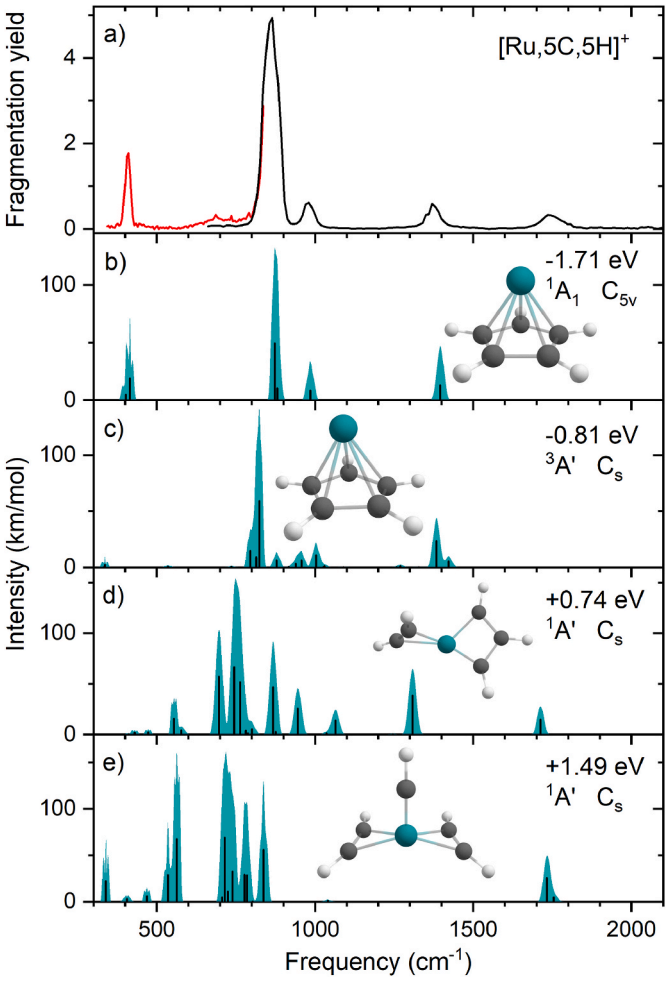

Fig. 6. a) Experimental IRMPD spectrum of $[Ru,5C,5H]^+$. The red and black traces were recorded using different FEL settings. b–e) Calculated IR spectra of $[Ru,5C,5H]^+$ isomers including rovibrational simulations at room temperature. Simulations are accompanied by molecular structures, electronic states, point groups, and theoretical energies relative to the Ru^+ + 2 *c*-C_3H_6 reactants.

The assigned $Ru(\eta^5\text{-}c\text{-}C_5H_5)^+$ ($^1A_1$) species is very symmetric with its C_{5v} point group, but the cyclopentadienyl ligand is not planar, as the hydrogen atoms are pulled 0.023 Å out of the cyclopentadienyl plane toward the Ru^+ ion. The five C–C, C–H, and Ru–C bond lengths are 1.433, 1.079, and 2.116 Å, respectively, with the Ru^+ ion located 1.730 Å above the center of the carbon ring. These distances are comparable to the free cyclopentadienyl with C_{2v} symmetry, having C–C bond lengths of 1.355 (2), 1.395 (2), and 1.466 Å and C–H bond lengths of 1.077, 1.078 (2), and 1.080 (2) Å. Again, a significant charge transfer has taken place with Ru charges of +0.396 e, +0.274 e, and +0.557 e according to Mulliken, APT, and NBO charge analyses, respectively.

3.7. Mechanism for C–H bond activation and C–C bond coupling by Ru^+

To further evaluate the interesting observation that reactions with two molecules of methane can lead to C–H bond activation and C–C bond coupling by the ruthenium cation, the potential energy surfaces for this reaction on both quartet and doublet spin surfaces were explored at the B3LYP/def2-TZVPPD level of theory. At this level of theory, a spin-contaminated doublet state ($S^2 = 1.75$) of Ru^+ is calculated to lie 0.83 eV above the ground state. An uncontaminated ($S^2 = 0.75$) ^2G ($4d^7$) state of Ru^+ is calculated to lie 1.71 eV above the ^4F ($4d^7$) ground state. This energy is higher than the experimental value of 1.25 eV (average over all spin-orbit levels) probably because the calculation mixes in ^2P ($4d^7$), ^2D ($4d^7$), and ^2H ($4d^7$) character and these states lie up to 2.11 eV above the ground level [40].

The initial C–H bond activations are shown in Fig. 7a. Ligation of Ru^+ (^4F) by two methane molecules is exothermic and barrierless, with binding energies of 0.78 and 0.66 eV for the first and second ligand, respectively. On the doublet spin surface, the initial methane complexation is much more exothermic (1.77 eV) because the low-spin empties an acceptor orbital on the Ru^+ center. The second methane molecule has a binding energy of 0.80 eV, more comparable to those on the quartet spin surface.

From the $Ru(CH_4)_2^+$ complexes, C–H bond activation leads to the inserted $HRuCH_3(CH_4)^+$ intermediate. Alternatively (dashed lines), the C–H bond activation could occur with only one methane ligand present, forming $HRuCH_3^+$, followed by methane complexation. However, starting with complexation of both methane molecules is the lower energy pathway. Notably, the $HRuCH_3(CH_4)^+$ intermediates of quartet and doublet spin are similar in energy: 0.82 and 0.69 eV, respectively, below the reactants, such that coupling between the two surfaces seems feasible at this point.

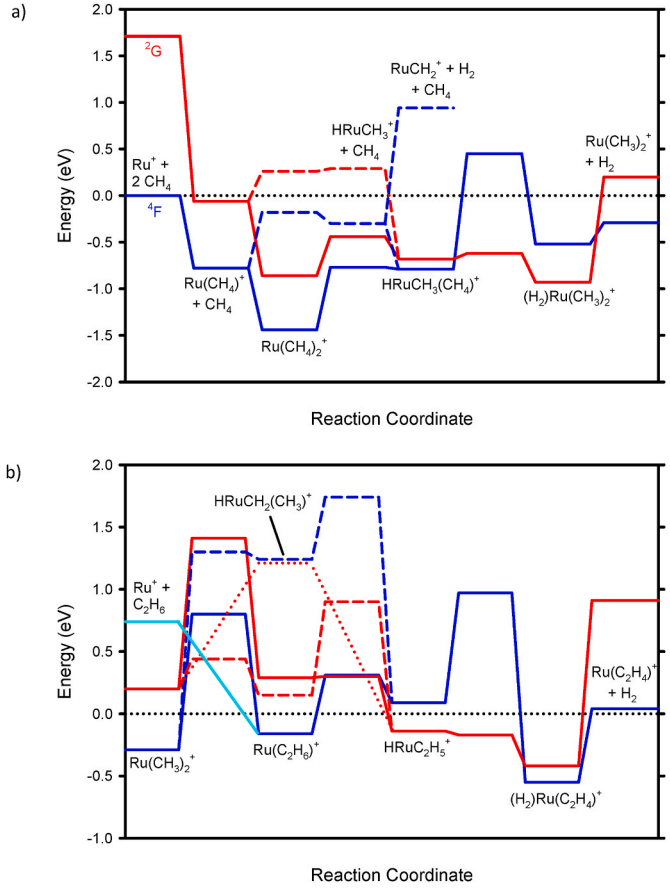

Fig. 7. Potential energy surfaces calculated at the B3LYP/def2-TZVPPD level of theory. Quartet and doublet spin surfaces are shown in blue and red, respectively. Part a) shows steps associated with the first dehydrogenation and part b) shows steps for the second dehydrogenation. The energy scale of part b includes the initial H_2 product.

From these intermediates, C–H bond activation of the second methane ligand leads to a ruthenium dimethyl cation dihydrogen intermediate, $(H_2)Ru(CH_3)_2^+$. The doublet spin species lies lower in energy than the quartet spin analog (by 0.41 eV) because the quartet spin species has no empty orbital to accept electron density from the H_2 ligand, whereas the 5s orbital is empty in the doublet spin analog. Because this orbital is occupied in the quartet spin species, this leads to a much higher barrier for the second C–H bond activation process along the quartet surface. In contrast, once the H_2 ligand is lost, the $Ru(CH_3)_2^+$ product prefers the quartet spin state (by 0.49 eV), reflecting the much lower energy of Ru^+ (^4F) versus Ru^+ (^2G). Overall, the first dehydrogenation can occur from ground state Ru^+ (^4F) + 2 CH_4 reactants without a barrier by coupling between the quartet and doublet surfaces.

We also explored an alternative pathway from $Ru(CH_4)_2^+$ in which the first dehydrogenation occurs from only one methane ligand, forming $RuCH_2(CH_4)^+$ instead of $Ru(CH_3)_2^+$. This path is shown in the Supporting Information, Fig. S11. It largely parallels the path shown in Fig. 7 but lies higher in energy for both the quartet and doublet spin states. Conceivably, it might also be possible to dehydrogenate one methane first, forming $RuCH_2^+$ ($^4B_2$), which then reacts with a second methane to yield $RuCH_2(CH_4)^+$. Experimentally, this first dehydrogenation step has been measured to require 1.17 ± 0.05 eV [15,22] (calculated here and previously as 0.94 eV) [15], an energy that surpasses those calculated for the interaction with two methane molecules. Thus, this pathway is likely to be less important than those shown in Fig. 7. Notably, this initial dehydrogenation reaction also appears to involve facile coupling between the reactant quartet spin surface and the doublet spin surface [15].

Fig. 7b shows the steps required to dehydrogenate $Ru(CH_3)_2^+$ and couple the two carbons on the same energy scale, i.e., relative to ground state Ru^+ (^4F) + 2 CH_4 reactants. Three possible pathways forming $HRuC_2H_5^+$ are shown. In pathway I (solid line), the two methyl groups couple to form a C–C bond and the $Ru(C_2H_6)^+$ intermediate. This is followed by C–H bond activation yielding the ethyl hydride intermediate, $HRuC_2H_5^+$. Both transition state energies relative to the associated dimethyl intermediate are comparable on the quartet and doublet spin surfaces, although the $HRuC_2H_5^+$ intermediate is lower in energy on the doublet surface (by 0.23 eV). In pathway II (dashed line), C–H bond activation from $Ru(CH_3)_2^+$ leads to a $HRuCH_2(CH_3)^+$ intermediate, which is much more stable on the doublet surfaces as this allows covalent bonding to all three ligands. This is followed by C–C coupling to yield the ethyl ligand. A third alternative (Pathway III, dotted line) was located on the doublet surface only, where attempts to locate a quartet spin analog failed. Pathway III directly couples the $Ru(CH_3)_2^+$ and $HRuC_2H_5^+$ intermediate, in essence by allowing a CH_2 ligand to switch between covalent bonding to H versus CH_3 (and synchronously changing the covalent bond to Ru from CH_3 to H). A fourth pathway (IV, Fig. S11) starts from $RuCH_2(CH_4)^+$ and then activates a C–H bond of the methane ligand to form $HRuCH_2(CH_3)^+$, rejoining pathway II. Pathway IV requires slightly more energy than Pathway II and eventually is limited by the same transition state linking $HRuCH_2(CH_3)^+$ and $HRuC_2H_5^+$. We also considered whether the $HRuCH_2(CH_3)^+$ intermediate might dehydrogenate by passing through a $(H_2)Ru(CH_2)_2^+$ intermediate and then undergoing C–C bond coupling. This was computationally investigated along the lower doublet spin surface and found to lie much higher in energy than Pathway II.

Of these various pathways, the lowest is Pathway I through the $Ru(C_2H_6)^+$ intermediate on the quartet surface, where the rate-limiting (C–C coupling) TS is 0.80 eV above the Ru^+ (^4F) + 2 CH_4 reactants. On the doublet surface, the lowest energy Pathway II proceeds through the $HRuCH_2(CH_3)^+$ intermediate, where the rate-limiting (C–C coupling) TS is 0.90 eV above ground state reactants.

Once the $HRuC_2H_5^+$ (^2A) intermediate (0.14 eV below reactants) is formed, it spontaneously can activate a terminal C–H bond to yield $(H_2)Ru(C_2H_4)^+$. The associated TS lies 0.03 eV below $HRuC_2H_5^+$ (0.04 eV above before zero-point energy corrections). On the quartet surface, the C–H bond activation step requires much more energy, but the final intermediate is 0.13 eV below the doublet spin analog. This seems like another place where coupling between the spin states is feasible, thereby allowing facile loss of the H_2 ligand to form the final $Ru(C_2H_4)^+$ ($^4B_2$) + $2H_2$ products, only 0.04 eV above the ground state reactants. The $Ru(C_2H_4)^+$ ($^2A_1$) + $2H_2$ products lie another 0.87 eV higher in energy.

Also shown in Fig. 7b is the energy of Ru^+ (^4F) + C_2H_6 + H_2 products (0.74 eV above ground state reactants, 0.67 eV from experiment). It seems feasible that this product (which we would not be sensitive to experimentally) could compete with the C–C coupling reactions. The main reason for including this asymptote here is that the reaction of Ru^+ (^4F) with ethane is known to undergo dehydrogenation in an exothermic, barrierless process with 100 % efficiency at thermal energies [22]. According to the surfaces shown, this cannot occur if the reaction remains on the quartet spin surface as the dehydrogenation step has a barrier that lies 0.23 eV above the Ru^+ + C_2H_6 reactants. This result is therefore an indication that coupling between the quartet and doublet surfaces must be reasonably facile. Indeed, the energy dependence of the cross section for this dehydrogenation reaction has been reported as $E^{-0.8}$ [22], which is a more rapid decline with energy than expected from the Langevin-Gioumousis-Stevenson collision model, $E^{-0.5}$. This observation is consistent with the energy dependence expected for a spin-crossing (approximately another factor of $E^{-0.5}$) [47].

4. Discussion and conclusion

The reaction between methane and Ru^+ ions yielded the $[Ru,2C,4H]^+$ and $[Ru,4C,6H]^+$ products, which we spectroscopically identified as $Ru(C_2H_4)^+$, with an ethene ligand, and $Ru(\eta^4$-*cis*-1,3-butadiene$)^+$. It is known that dehydrogenation of one methane by Ru^+ to form $RuCH_2^+$ + H_2 is endothermic by 1.17 ± 0.05 eV [15]. Thus, the observation of products containing solely even numbers of carbon atoms when reacting with methane implies that dehydrogenation is initiated by the energy released during the adsorption of two methane molecules. Because the reaction of Ru^+ with methane at thermal energies and relatively high pressures was earlier observed to solely form the adducts $[Ru,C,4H]^+$ and $[Ru,2C,4H_4]^+$ [13], we conclude that the reaction conditions in our room temperature experiments at relatively low pressures allows for the conservation of (part of) the adsorption energy for both adsorptions. The observation that the reactions require relatively high methane pressures and did not benefit from Ar in the quadrupole ion trap indicates that the reactions are relatively inefficient, hinting at an isoenergetic or endothermic barrier for the dehydrogenation of two methane molecules. This conclusion is consistent with the calculated potential energy surface for formation of $Ru(C_2H_4)^+$ + $2H_2$, which identified C–C coupling from $Ru(CH_3)_2^+$ to $Ru(C_2H_6)^+$ to be the rate-limiting TS at 0.80 eV above the energy of the ground state reactants. Such a barrier could be overcome if at least a part of the ion population is warmer than room temperature as a result of residual kinetic energy upon entering the trap or that the original Ru^+ reactant is formed in an excited electronic state. That these are relevant considerations is evidenced by the observation of an endothermically formed Ru(*cis*-1,3-butadiene)$^+$ product, with a calculated endothermicity of 1.16 eV relative to Ru^+ (^4F) + 4 CH_4.

The reaction between Ru^+ and *c*-C_3H_6 shows more reaction products compared to methane, clearly a consequence of releasing the ring-strain energy. We spectroscopically identified the dehydrogenation product $[Ru,3C,4H]^+$ as $Ru(\eta^2$-propyne$)^+$, the $[Ru,2C,2H]^+$ species as $Ru(C_2H_2)^+$ containing an ethyne ligand, and the $[Ru,5C,5H]^+$ species as $Ru(\eta^5$-*c*-$C_5H_5)^+$. These three products are formed in reactions that are exothermic by more than 1 eV.

All observed products contain ligands that are distorted from the free molecule by Ru^+. The binding energies are calculated to range from 2.0 to 4.4 eV and are associated with electron density donation from the ligand to the Ru^+ ion. This indicates at least partial activation of the ligands in all cases. The charge on the ruthenium atom averaged over the Mulliken and APT methods depends on the ligand size, with the charge on Ru decreasing as the ligand size increases. Specifically, we found +0.65 e, +0.64 e, +0.55 e, +0.40 e, and +0.34 e on Ru in the $Ru(C_2H_2)^+$, $Ru(C_2H_4)^+$, Ru(propyne)$^+$, Ru(*cis*-1,3-butadiene)$^+$, and Ru(*c*-$C_5H_5)^+$ species, respectively. The NBO analysis finds less electron transfer with charges on Ru of +0.97 e, +0.97 e, +0.92 e, +0.71 e, and +0.56 e, respectively. Note that the charges for the ethyne and ethene ligands are similar, consistent with Ru interacting primarily with only one of the π bonds of ethyne. Likewise, the propyne ligand exhibits more electron donation than ethyne, consistent with the electron donating ability of the additional methyl group in propyne. The larger C_4H_6 and C_5H_5 ligands donate progressively more electrons to the metal cation.

Examination of the molecular orbitals (MOs) of the $Ru(C_2H_2)^+$ and $Ru(C_2H_4)^+$ complexes shows some subtle differences. The orbital occupations in both are fairly similar with doubly occupied $4d_{z2}$–π_{ip}(CC) (ip = in-plane) and $4d_{yz}$–π^*_{ip}(CC) MOs, along with a singly occupied 5s-π_{ip}(CC) MO where the RuCC atoms lie in the yz plane and the z axis is the symmetry axis. As noted above, the δ-like $4d_{xy}$ and $4d_{x2-y2}$ MOs are singly and doubly occupied in the ground state, with a near-isoenergetic state if their occupancies are swapped. The singly occupied $4d_{xz}$ orbital, which has the symmetry to interact with the out-of-plane (oop) π orbital of ethyne, has a different character for the ethyne and ethene ligand complexes. The oop electron density of the ethene ligand is primarily located in the localized C–H bonds that are remote from the $4d_{xz}$ orbital, which thus becomes a non-bonding orbital. In contrast, the ethyne ligand with its π_{oop} bond has a much more delocalized electron cloud that does interact with the $4d_{xz}$ orbital in an antibonding fashion.

In previous work, we demonstrated the formation of ethene from the reaction of two methane molecules with Pt^+ yielding a $Pt(C_2H_4)^+$ complex [19]. The C═C bond length of 1.325 Å in free ethene was calculated to increase to 1.390 Å in $Ru(C_2H_4)^+$, whereas a value of 1.402 Å was found for $Pt(C_2H_4)^+$. The Ru^+ ion was determined to be 2.069 Å from the center of ethene's C═C bond, whereas this distance was only 2.036 Å for the Pt^+ complex, even though the Pt^+ atomic ion is larger than Ru^+. In general, these numbers suggest that the interaction between ethene and Pt^+ is stronger than the interaction between ethene and Ru^+. Indeed, the direct elimination of ethene from $Ru(C_2H_4)^+$ is calculated to require 2.00 eV instead of 2.94 eV calculated for direct ethene elimination from $Pt(C_2H_4)^+$. Therefore, it is easier to eliminate ethene from Ru^+ compared to Pt^+, which could be beneficial for catalytic properties.

In summary, methane and cyclopropane were reacted with Ru^+ ions in a room temperature quadrupole ion trap. In the reaction with methane, we observed $[Ru,2C,4H]^+$ and $[Ru,4C,6H]^+$ species. These were spectroscopically identified to be $Ru(C_2H_4)^+$ containing an ethene ligand and as $Ru(\eta^4$-*cis*-1,3-butadiene$)^+$. The reactions leading to these products are calculated to be nearly thermoneutral and endothermic by 1.16 eV, respectively. In the reaction with cyclopropane, several species were observed. Those spectroscopically investigated included the dehydrogenation product of *c*-C_3H_6, $[Ru,3C,4H]^+$, identified as $Ru(\eta^2$-propyne$)^+$, $[Ru,2C,2H]^+$ as $Ru(C_2H_2)^+$ containing an ethyne ligand, and $[Ru,5C,5H]^+$ as $Ru(\eta^5$-*c*-$C_5H_5)^+$ with a cyclopentadienyl ligand. These species were all formed in reactions that are exothermic by more than 1 eV.

Notes

The data supporting the findings of this study are stored on the Radboud Data Repository and will be made available upon request.

Declaration of competing interest

The authors declare that they have no known competing financial interests or personal relationships that could have appeared to influence the work reported in this paper.

Data availability

Data will be made available on request.

Acknowledgments

This work was funded by NWO's Materials for Sustainability program (grant no. 739.017.008). We gratefully acknowledge the Nederlandse Organisatie voor Wetenschappelijk Onderzoek (NWO) for the support of the FELIX Laboratory and for CPU time on the Dutch National Supercomputers Cartesius and Snellius (project number 2021.055). Additional financial support was provided by the National Science Foundation (grant no. CHE-2313553).

Appendix A. Supplementary data

Supplementary data to this article can be found online at https://doi.org/10.1016/j.ijms.2023.117165.

References

[1] K. Aasberg-Petersen, I. Dybkjær, C.V. Ovesen, N.C. Schjødt, J. Sehested, S. G. Thomsen, Natural gas to synthesis gas - catalysts and catalytic processes, J. Nat. Gas Sci. Eng. 3 (2011) 423–459.
[2] W. Ma, A.K. Dalai, Effects of structure and particle size of iron, cobalt and ruthenium catalysts on fischer–tropsch synthesis, Reactions 2 (2021) 62–77.
[3] A.I. Olivos-Suarez, À. Szécsényi, E.J.M. Hensen, J. Ruiz-Martinez, E.A. Pidko, J. Gascon, Strategies for the direct catalytic valorization of methane using heterogeneous catalysis: challenges and opportunities, ACS Catal. 6 (2016) 2965–2981.
[4] R.H. Crabtree, Organometallic alkane CH activation, J. Organomet. Chem. 689 (2004) 4083–4091.
[5] K.K. Irikura, W.A. Goddard, W.A. Goddard III, Energetics of 3rd-row transition-metal methylidene ions MCH2+ (M=La, Hf, Ta, W, Re, Os, Ir, Pt, Au), J. Am. Chem. Soc. 116 (1994) 8733–8740.
[6] J. Roithova, D. Schröder, Selective activation of alkanes by gas-phase metal Ions, Chem. Rev. 110 (2010) 1170–1211.
[7] P.B. Armentrout, Methane activation by 5d transition metals: energetics, mechanisms, and periodic trends, Chem. Eur J. 23 (2017) 10–18.
[8] K.K. Irikura, J.L. Beauchamp, Methane oligomerization in the gas phase by third-row transition-metal ions, J. Am. Chem. Soc. 113 (1991) 2769–2770.
[9] X.-G. Zhang, R. Liyanage, P.B. Armentrout, Potential energy surface for activation of methane by Pt^+ : a combined guided ion beam and DFT study, J. Am. Chem. Soc. 123 (2001) 5563–5575.
[10] P.B. Armentrout, S. Shin, R. Liyanage, Guided-ion beam and theoretical study of the potential energy surface for activation of methane by W^+, J. Phys. Chem. A 110 (2006) 1242–1260.
[11] F.X. Li, X.G. Zhang, P.B. Armentrout, The most reactive third-row transition metal: guided ion beam and theoretical studies of the activation of methane by Ir+, Int. J. Mass Spectrom. 255 (2006) 279–300.
[12] L.G. Parke, C.S. Hinton, P.B. Armentrout, Experimental and theoretical studies of the activation of methane by Ta^+, J. Phys. Chem. C 111 (2007) 17773–17787.
[13] A. Shayesteh, V.V. Lavrov, G.K. Koyanagi, D.K. Bohme, Reactions of atomic cations with methane: gas phase room-temperature kinetics and periodicities in reactivity, J. Phys. Chem. A 113 (2009) 5602–5611.
[14] P.B. Armentrout, L. Parke, C. Hinton, M. Citir, Activation of methane by Os^+ : guided-ion-beam and theoretical studies, Chempluschem 78 (2013) 1157–1173.
[15] P.B. Armentrout, Y.M. Chen, Activation of methane by Ru^+: experimental and theoretical studies of the thermochemistry and mechanism, Int. J. Mass Spectrom. 413 (2017) 135–149.
[16] S.W. Buckner, T.J. MacMahon, G.D. Byrd, B.S. Freiser, Gas-phase reactions of Nb^+ and Ta^+ with alkanes and alkenes. C-H bond activation and ligand-coupling mechanisms, Inorg. Chem. 28 (1989) 3511–3518.
[17] M.R. Sievers, Y.M. Chen, C.L. Haynes, P.B. Armentrout, Activation of CH_4, C_2H_6, and C_3H_8 by gas-phase Nb^+ and the thermochemistry of Nb-ligand complexes, Int. J. Mass Spectrom. 195–196 (2000) 149–170.
[18] P.B. Armentrout, M.R. Sievers, Activation of CH_4 by gas-phase Zr^+ and the Thermochemistry of Zr-ligand complexes, J. Phys. Chem. A 107 (2003) 4396–4406.
[19] F.J. Wensink, N. Roos, J.M. Bakker, P.B. Armentrout, C–H bond activation and C–C coupling of methane on a single cationic platinum center: a spectroscopic and theoretical study, Inorg. Chem. 61 (2022) 11252–11260.
[20] O.W. Wheeler, M. Salem, A. Gao, J.M. Bakker, P.B. Armentrout, Activation of C–H bonds in $Pt^+ + x\ CH_4$ reactions, where x = 1–4: identification of the platinum dimethyl cation, J. Phys. Chem. A 120 (2016) 6216–6227.
[21] S. Liu, Z. Geng, Y. Wang, Y. Yan, DFT studies for dehydrogenation of methane by gas-phase Ru^+, Comput. Theor. Chem. 977 (2011) 44–49.
[22] P.B. Armentrout, Y.-M. Chen, Activation of C_2H_6, C_3H_8, $HC(CH_3)_3$, and c-C_3H_6 by gas-phase Ru and the thermochemistry of Ru-ligand complexes, J. Am. Soc. Mass Spectrom. 34 (1999) 821–839.
[23] B. Ruscic, R.E. Pinzon, G. Von Laszewski, D. Kodeboyina, A. Burcat, D. Leahy, D. Montoy, A.F. Wagner, Active thermochemical tables: thermochemistry for the 21st century, J. Phys. Conf. Ser. 16 (2005) 561–570.
[24] J. Roithová, J.M. Bakker, Ion spectroscopy in methane activation, Mass Spectrom. Rev. 41 (2022) 513–528.
[25] C. Berg, T. Schindler, G. Niedner-Schatteburg, V.E. Bondybey, Reactions of simple hydrocarbons with Nb_n^+: chemisorption and physisorption on ionized niobium clusters, J. Chem. Phys. 102 (1995) 4870–4884.
[26] F.J. Wensink, M.G. Münst, J. Heller, M. Ončák, J.M. Bakker, C. Van Der Linde, IR multiple photon dissociation spectroscopy of MO_2^+ (M = V, Nb, Ta), J. Chem. Phys. 153 (2020), 171101.
[27] S.D. Wiersma, A. Candian, J.M. Bakker, A. Petrignani, Gas-phase spectroscopy of photostable PAH ions from the mid- to far-infrared, Mon. Not. Roy. Astron. Soc. 516 (2022) 5216–5226.
[28] A. Petrignani, M. Vala, J.R. Eyler, A.G.G.M. Tielens, G. Berden, A.F.G. van der Meer, B. Redlich, J. Oomens, Breakdown products of gaseous polycyclic aromatic hydrocarbons investigated with infrared ion spectroscopy, Astrophys. J. 826 (2016) 33.
[29] A.G. Marshall, C.L. Hendrickson, G.S. Jackson, Fourier transform ion cyclotron resonance mass spectrometry: a primer, Mass Spectrom. Rev. 17 (1998) 1–35.
[30] M.J. Frisch, G.W. Trucks, H.B. Schlegel, G.E. Scuseria, M.A. Robb, J.R. Cheeseman, G. Scalmani, V. Barone, G.A. Petersson, H. Nakatsuji, X. Li, M. Caricato, A. V. Marenich, J. Bloino, B.G. Janesko, R. Gomperts, B. Mennucci, D.J. Hratch, Gaussian 16, Revision C.01, Gaussian, Inc., Wallingford CT, 2016.
[31] A.D. Becke, Density-functional thermochemistry. III. The role of exact exchange, J. Chem. Phys. 98 (1993) 5648–5652.
[32] C. Lee, W. Yang, R.G. Parr, Development of the Colle-Salvetti correlation-energy formula into a functional of the electron density, Phys. Rev. B 37 (1988) 785–789.
[33] P.B. Armentrout, S.E.J. Kuijpers, O. V Lushchikova, R.L. Hightower, G.C. Boles, J. M. Bakker, Spectroscopic identification of the carbyne hydride structure of the dehydrogenation product of methane activation by osmium cations, J. Am. Soc. Mass Spectrom. 29 (2018) 1781–1790.
[34] J.M. Bakker, C.J. Owen, S.W. Nooteboom, O.V. Lushchikova, P.B. Armentrout, Structural characterization of $[M,C,2H]^+$ products formed by reaction of 5d metal cations Pt^+ and Ir^+ with ethylene oxide and Ta^+ with methane using messenger spectroscopy, J. Mol. Spectrosc. 378 (2021), 111472.
[35] V.J.F. Lapoutre, B. Redlich, A.F.G. van der Meer, J. Oomens, J.M. Bakker, A. Sweeney, A. Mookherjee, P.B. Armentrout, Structures of the dehydrogenation products of methane activation by 5d transition metal cations, J. Phys. Chem. A 117 (2013) 4115–4126.
[36] O.W. Wheeler, M. Salem, A. Gao, J.M. Bakker, P.B. Armentrout, Sequential activation of methane by Ir^+: an IRMPD and theoretical investigation, Int. J. Mass Spectrom. 435 (2019) 78–92.
[37] P.B. Armentrout, B.C. Stevenson, F. Yang, F.J. Wensink, O.V. Lushchikova, J. M. Bakker, Infrared spectroscopy of gold carbene cation ($AuCH_2^+$): covalent or dative bonding? J. Phys. Chem. A 123 (2019) 8932–8941.
[38] C.L. Haynes, Y.-M. Chen, P.B. Armentrout, Reaction of $FeCH_2^+ + D_2$: probing the $[FeCH_4]^+$ potential energy surface, J. Phys. Chem. 100 (1996) 111–119.
[39] W.L. Meerts, M. Schmitt, Application of genetic algorithms in automated assignments of high-resolution spectra, Int. Rev. Phys. Chem. 25 (2006) 353–406.
[40] A. Kramida, Y. Ralchenko, J. Reader, NIST ASD Team, NIST Atomic Spectra Database, 2022 ver. 5.10).
[41] T. Shimanouchi, Tables of molecular vibrational frequencies. Consolidated volume I, Natl. Bur. Stand. (1972) 1–160.
[42] R.S. Mulliken, Electronic population analysis on LCAO–MO molecular wave functions. I, J. Chem. Phys. 23 (1955) 1833–1840.
[43] W.B. Person, J.H. Newton, Dipole moment derivatives and infrared intensities. I. Polar tensors, J. Chem. Phys. 61 (1974) 1040–1049.
[44] A.E. Reed, L.A. Curtiss, F. Weinhold, Intermolecular interactions from a natural bond orbital, donor-acceptor viewpoint, Chem. Rev. 88 (1988) 899–926.
[45] E.D. Glendening, A.E. Reed, J.E. Carpenter, F. Weinhold, NBO Version 3.1, Gaussian Inc., Pittsburgh, 2003.
[46] Ò. González-Blanco, V. Branchadell, R. Grée, Structure and conformational equilibrium in substituted [(η^4-butadiene)Fe(CO)$_3$] complexes: a density functional study, Chem. Eur J. 5 (1999) 1722–1727.
[47] C. Rue, P.B. Armentrout, I. Kretzschmar, D. Schröder, J.N. Harvey, H. Schwarz, Kinetic-energy dependence of competitive spin-allowed and spin-forbidden reactions: $V^+ + CS_2$, J. Chem. Phys. 110 (1999) 7858–7870.